PHYSICAL REVIEW A **91**, 042709 (2015)

Classical description of H(1s) and H*($n = 2$) for cross-section calculations relevant to charge-exchange diagnostics

N. D. Cariatore,[1] S. Otranto,[1] and R. E. Olson[2]
[1] *IFISUR and Dto. de Física, Universidad Nacional del Sur, 8000 Bahía Blanca, Argentina*
[2] *Physics Department, Missouri University of Science and Technology, Rolla, Missouri 65401, USA*

(Received 20 February 2015; published 28 April 2015)

In this work, we introduce a classical trajectory Monte Carlo (CTMC) methodology, specially conceived to provide a more accurate representation of charge-exchange processes between highly charged ions and H(1s) and H*($n = 2$). These processes are of particular relevance in power fusion reactor programs, for which charge-exchange spectroscopy has become a useful plasma diagnostics tool. To test the methodology, electron-capture reactions from these targets by C^{6+}, N^{7+}, and O^{8+} are studied at impact energies in the 10–150 keV/amu range. State-selective cross sections are contrasted with those predicted by the standard microcanonical formulation of the CTMC method, the CTMC method with an energy variation of initial binding energies that produces an improved radial electron density, and the atomic orbital close-coupling method. The present results are found in to be much better agreement with the quantum-mechanical results than the results of former formulations of the CTMC method.

DOI: 10.1103/PhysRevA.91.042709 PACS number(s): 34.70.+e, 32.30.Rj, 32.30.Jc

I. INTRODUCTION

For nearly five decades since its proposal [1], the classical trajectory Monte Carlo (CTMC) method has been extensively used to provide theoretical insight for many atomic and molecular collision processes with ions and electrons. Being the simplest target to consider, atomic hydrogen was used to test the methodology by the late 1970s. Charge exchange and ionization processes following collisions of multiply charged ions with H(1s) collisions were scrutinized at the total-cross-section level by Olson and Salop [2] and soon after at the (n,l) state-selective level by Olson [3]. Since then, multiple works have been published on CTMC studies of charge-exchange and ionization processes on H(1s) involving either bare or partially stripped projectiles at different impact energies (see Ref. [4] for a topical review).

The success of the CTMC method can be considered quite remarkable, since this method relies exclusively on Newton's physical laws to describe physical processes which take place in the quantum-mechanical domain. In particular, the success evidenced by the methodology for charge-exchange studies on H(1s) has been at some extent attributed to the fact that the classical and quantum-mechanical momentum distributions for the target electron are identical. However, this is not the case for the radial distribution provided by the microcanonical phase-space distribution used to initialize the target system. The classical radial distribution has a finite range, leading to a clear underestimation of the contributions to ionization, charge exchange, and excitation channels at larger impact parameters of the projectile.

In order to circumvent this issue, Eichenauer *et al.* (1981) proposed the cut-off Wigner-phase-space distribution which yielded an improved radial distribution at the expense of losing the exact momentum distribution [5]. Soon after, and in line with Eichenauer's arguments, Hardie and Olson (1983) [6] proposed a discrete summation of microcanonical ensembles corresponding to different binding energies for the target electron (this method is hereafter referred to as hydrogenic-E-CTMC). In their method, the discrete summation is determined by requiring the reproduction of the exact quantum-mechanical H(1s) radial distribution. This is achieved by weighting each energy component with a coefficient that is determined by a least-squares fitting procedure. The correct quantal distribution is statistically recovered at the expense of considering a finite set of ionization potentials within the range 0.125–2.0 a.u. As the ionization potential increases, the maximum impact parameter that contributes to the charge-exchange process $b_{\max}$ decreases. Hence, by using a discrete basis, considerable computer time is saved since the range of impact parameters for each set can be optimized. Moreover, this procedure still provides a good approximation to the correct momentum distribution. Eichenauer's studies were also followed by Cohen, who later published another classical phase-space function which leads to the exact quantum-mechanical radial distribution and provides a good approximation to the quantum-mechanical momentum distribution [7].

Throughout the years, interest also moved to multielectronic targets and CTMC studies also tackled multiple electron processes like multiple capture, multiple ionization, and transfer ionization. CTMC methods that explicitly account for many electrons in atomic [8–13] and molecular systems [14–17] have been also developed and provide physical descriptions that extend beyond those provided by the independent-electron and independent-event approximations.

The power fusion reactor programs (JET [18] and ITER [19]), on the other hand, kept alive the interest in the much simpler atomic hydrogen system to the present. Most of the actual needs in this direction point towards the use of charge-exchange spectroscopy (CXS) as a potential tool for plasma diagnostics [20,21]. For this task, reliable charge-exchange cross sections are needed to model effective emission coefficients at plasma temperatures of about 10 keV/amu to those encountered during neutral beam heating of about 50keV/amu [21,22].

It is worth noting that CXS relies on the photonic emission in the visible range (1.771 to 3.1 eV). This limitation arises from the use of fiber optics to extract the spectra from the nuclear vessel. Since charge-exchange cross sections from $H^*(n=2)$ are larger than those from $H(1s)$ by orders of magnitude, even a tiny fraction of $H^*(n=2)$ present in the plasma ($<1\%$) dominates the visible range photonic emission for impact energies up to a few tens of keV/amu [23]. Hence, collisional data on $H^*(n=2)$ are also needed in order to obtain accurate emission coefficients.

Besides the CTMC method, quantum-mechanical methods like atomic-orbital expansions [24] and the atomic-orbital close-coupling method (AOCC) [25–27] have provided assistance on this task. These time-dependent methods rely on huge basis sets to properly describe the collision. In this sense, highly charged projectiles, and/or targets with low ionization potentials, which populate high-lying states of the projectile, still represent a remarkable computational challenge.

In this work, we introduce an alternative CTMC model for $H(1s)$ and $H^*(n=2)$ (hereafter referred to as hydrogenic-Z-CTMC) which provides a more accurate representation of the target system than the microcanonical ensemble. While it follows the hydrogenic-E-CTMC spirit, the hydrogenic-Z-CTMC model reproduces the exact momentum distribution and the correct exponential tails in the radial distributions. This is achieved by considering different target nuclear charges (Z) while retaining the correct ionization potential (V_{ion}) for the target under consideration. Thus, the method is consistent with established binning procedures to yield (n,l) cross sections, unlike that of the hydrogenic-E-CTMC method. The projectiles considered throughout this work to test the model are C^{6+}, N^{7+}, and O^{8+}, which are projectiles of high interest to the fusion reactor community.

In Sec. II we introduce the model and describe the radial and momentum distributions obtained with this method. In Sec. III A, results for $H(1s)$ are shown and contrasted with the microcanonical and hydrogenic-E-CTMC models as well as to recently reported AOCC results [26,27]. In Sec. III B we explicitly consider the $H^*(n=2)$ case. Line-emission cross sections are presented and analyzed in Sec. III C. Finally, in Sec. V, conclusions and outlooks are shown.

II. THEORETICAL METHOD

In the CTMC method, Hamilton's equations are numerically solved by means of a fourth-order Runge–Kutta integration method with an adaptive step size. At the beginning of the simulation, the target electron evolves under the sole Coulomb field of the proton. Classical return points for $H(1s)$ and $H^*(n=2)$ read $r\sim 2.0$ a.u. and $r\sim 8.0$ a.u. respectively. Details on the initialization procedures for the standard microcanonical CTMC and the hydrogenic-E-CTMC methods can be found in Refs. [2,6,28] respectively, as in many subsequent works.

In the present hydrogenic-Z-CTMC method, each event is initialized by sorting over the quantum-mechanical momentum distribution for $H(1s)$, $H^*(2s)$, or $H^*(2p)$. An associated radial coordinate value is obtained via the energy equation for the target which includes a potential-energy term which is proportional to the nuclear charge Z. By keeping the ionization potential as a fixed parameter, we approximate the quantum-mechanical radial distribution as a sum of classical radial distributions $\rho(r)$ as

$$\rho(r)=\sum_i \alpha_i \rho(r,Z_i). \tag{1}$$

Here, α_i are the weight factors for the different distributions associated with the different Z values considered. These factors are calculated by a least-squares fitting procedure.

TABLE I. Hydrogenic-Z-CTMC weight factors (α_i) for the orbitals $1s$, $2s$, and $2p$.

	α_i		
Z_i	$1s$	$2s$	$2p$
0.500	0.072 40	0.063 96	
0.625	0.076 58	0.142 80	
0.690			0.256 48
0.750	0.096 65	0.202 70	
0.875	0.092 30	0.185 86	0.063 18
1.000	0.162 04	0.161 71	0.345 04
1.125		0.120 56	
1.250	0.179 71	0.083 84	
1.375		0.050 37	0.312 96
1.500	0.130 19	0.043 27	0.000 17
1.750	0.080 71	0.028 56	0.028 18
2.000	0.064 75		0.027 69
2.500	0.044 93		

In Table I, we present the values of Z_i and α_i used in this work for the $1s$, $2s$, and $2p$ orbitals of hydrogen. The corresponding momentum and radial distributions obtained for these orbitals are explicitly shown in Fig. 1. As already recognized in previous works for argon targets [29,30], by sorting over the quantum-mechanical momentum distribution, nodal structures in the radial distribution can be classically reproduced. This is also noticeable in the present hydrogenic-Z-CTMC method. In particular, the nodal structure for the $2s$ state radial distribution is qualitatively reproduced by the present set of weight factors which are constrained to take positive values only. Note that, in the trajectory calculations, the nuclear charge of the target is maintained at $+1$ for the projectile-target nuclear-nuclear interaction to preclude an unphysical repulsive interaction in the initial channel.

A classical number n_c is obtained from the binding energy E_p of the electron relative to the projectile by

$$E_p=-Z_p^2/\left(2n_c^2\right), \tag{2}$$

where Z_p is the charge of the projectile core. These classical n_c values are then related to the specific quantum level n according to the relationship derived by Becker and MacKellar [31],

$$[(n-1)(n-1/2)n]^{1/3}\leqslant n_c<[n(n+1/2)(n+1)]^{1/3}. \tag{3}$$

From the normalized classical angular momentum $\mathbf{l_c}=(n/n_c)(\mathbf{r}\times\mathbf{k})$, where $\mathbf{r}$ and $\mathbf{k}$ are the captured electron position and momentum, respectively, relative to the projectile, we relate l_c to the orbital quantum number l of the final state by

$$l\leqslant l_c\leqslant l+1. \tag{4}$$

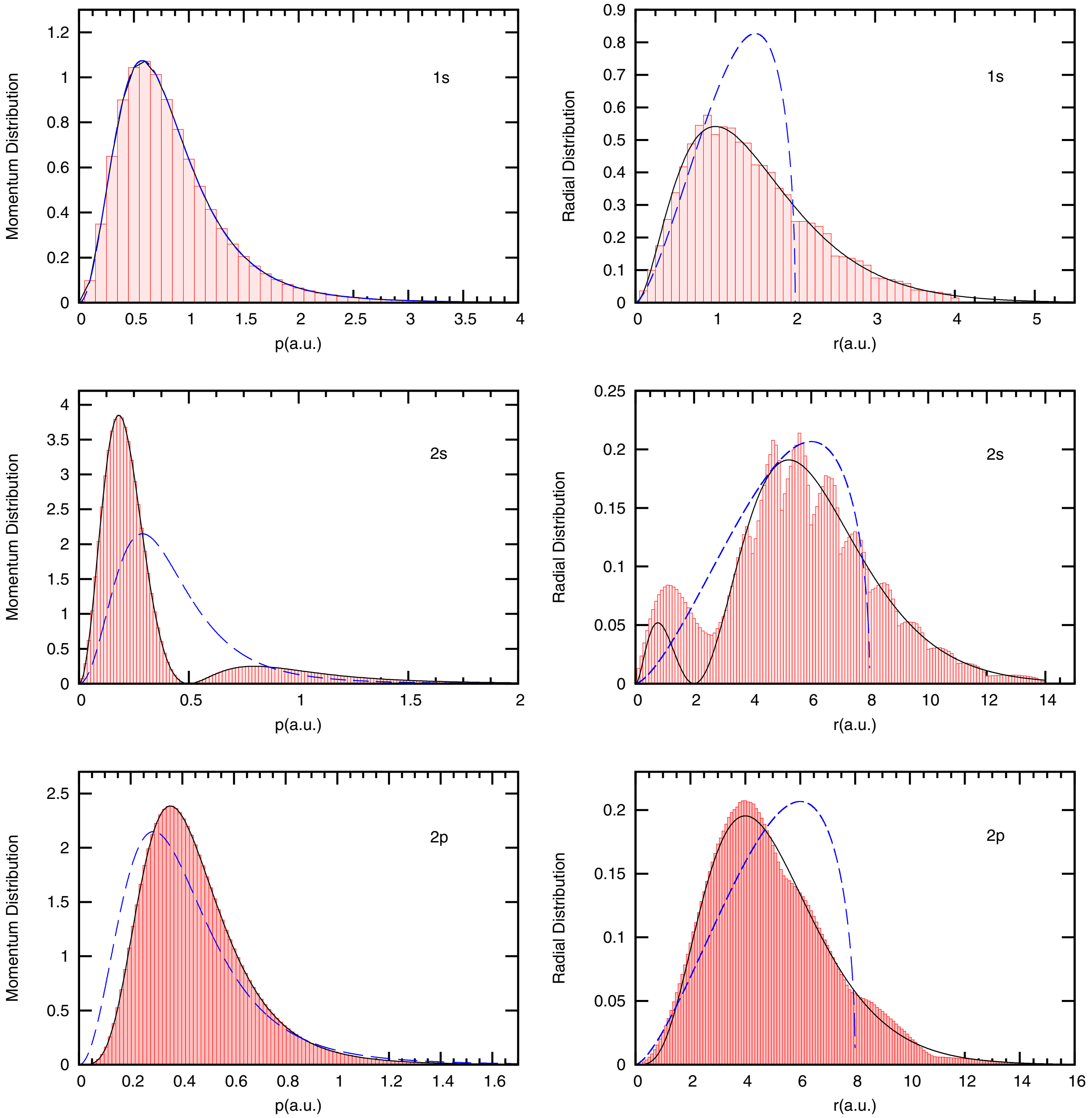

FIG. 1. (Color online) Momentum and radial distributions for $1s$, $2s$, and $2p$ orbitals. Black solid line shows the quantum-mechanical distributions, blue-dashed line shows the microcanonical distributions, and red columns present the hydrogenic-Z-CTMC distributions.

The total cross section for a given process τ (which represents either capture, ionization, or excitation) is then defined by

$$\sigma^{\tau} = \sum_i \alpha_i \sigma_i^{\tau}, \tag{5}$$

where the cross sections σ_i^{τ} are given by

$$\sigma_i^{\tau} = \frac{N(\tau)}{N_{\mathrm{tot}}} \pi b_{\max}^2. \tag{6}$$

Here, $N(\tau)$ is the number of events associated with the process τ under study, N_{tot} is the total number of trajectories integrated, and $b_{\max}$ is the impact-parameter value beyond which the probability to collect events is negligibly small.

In order to obtain emission cross sections, $\sigma^{(\mathrm{em})}_{n,l,m\to n',l',m'}$, cascade contributions from higher $n'' > n$ levels are added, and the n, l, m_l populations are multiplied by hydrogenic branching ratios for the relevant transitions and by their relative line strengths [32].

Advantages of the present methodology compared to the hydrogenic-E-CTMC can be established *a priori*. Based on the fact that the most populated projectile n level in charge-exchange processes is given by the $\sqrt{13.6/V_{\mathrm{ion}}}q^{3/4}$ scaling law (where q is the projectile charge and V_{ion} is the ionization potential and is expressed in eV) [3], a methodology based on a set of microcanonical distributions involving different V_{ion} values is expected to lead to a wider overall n distribution. In contrast, the hydrogenic-Z-CTMC is expected to lead to a more accurate n distribution, provided that the correct V_{ion} value is considered in all the terms of the set. On the other hand, the introduction of different Z values could in principle affect the total number of charge-exchange events recorded, provided that, for a given V_{ion} value, as the target nuclear charge increases the charge-exchange probability diminishes. Such preliminary first-hand assessments must be tested via an exhaustive exploration of charge-exchange processes at different impact energies and projectile charges. That is the purpose of our next section.

An additional advantage of the present method against the hydrogenic-E-CTMC model would be provided by momentum spectroscopy measurements for the electron capture to the continuum process. While the new method would be consistent with experiments showing an abrupt rise in the recoil-ion longitudinal momentum distribution at the minimum possible value given by $p_{\text{long-min}} = -v_p/2 + V_{\mathrm{ion}}/v_p$ [33], for the hydrogenic-E-CTMC such a structure would be smeared. This results from the fact that the different terms the radial distribution is built upon, leading to sharp step rises at different recoil-ion longitudinal-momentum values. Those terms involving V_{ion} values lower (larger) than the V_{ion} of the target would shift $p_{\text{long-min}}$ to lower (larger) values.

III. RESULTS AND DISCUSSION

A. State-selective electron capture in C^{6+}, N^{7+}, and O^{8+} collisions on H(1*s*)

First, we compare the state-selective electron-capture cross sections provided by the present theoretical method for C^{6+}, N^{7+}, and O^{8+} collisions on H(1*s*) against those obtained by other existing methods. These latter methods are the standard microcanonical CTMC method, the hydrogenic-E-CTMC method, and the quantum-mechanical AOCC results of Igenbergs *et al.* [26,27]. In Fig. 2 we show the electron-capture cross sections to levels $n = 3$ to 8, $n = 3$ to 9, and $n = 3$ to 9 for C^{6+}, N^{7+}, and O^{8+}, respectively. These are represented as a function of impact energy in the 10–150 keV/amu range.

At impact energies greater than about 100 keV/amu, the predictions of the different methods are all in very good agreement with each other. At impact energies lower than about 40 keV/amu, on the other hand, the microcanonical and hydrogenic-E-CTMC predictions tend to depart from the AOCC results. Departures are more evident for n values greater than $n_{\max}$, which is the value at which the n distribution attains its maximum and is approximately given by the $\sqrt{13.6/V_{\mathrm{ion}}}q^{3/4}$ scaling law [3].

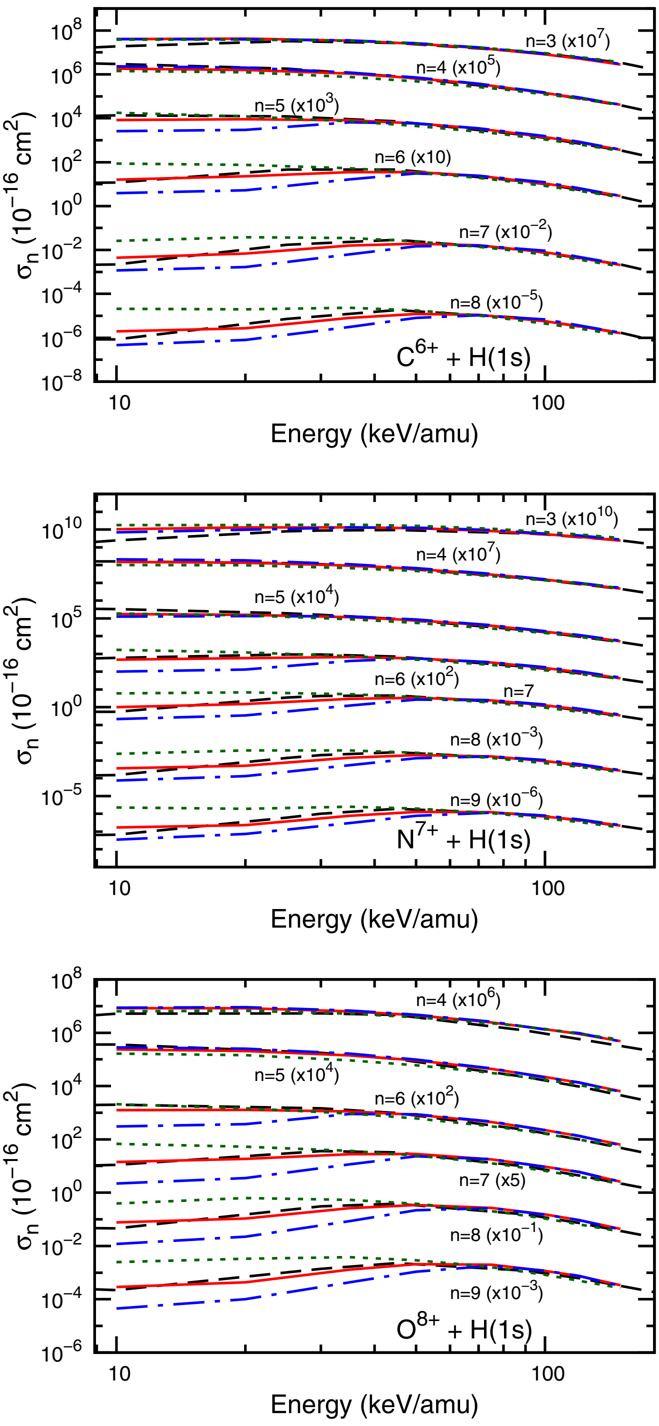

FIG. 2. (Color online) n-state-selective capture cross section as a function of the projectile energy following C^{6+}, N^{7+}, and O^{8+} collisions on H(1*s*). Red-solid line is hydrogenic-Z-CTMC, green-dotted line is hydrogenic-E-CTMC, blue dashed-dotted line is microcanonical-CTMC, black dashed line is AOCC data from Refs. [26,27].

At these low impact energies, the microcanonical description underestimates the AOCC results for the high-lying n levels; behavior that we relate to the classical compressed radial distribution. In contrast, the hydrogenic-E-CTMC method, which leads to an improved description of the radial distribution, leads to an overestimation of the population of the high-lying n values of the projectile. We relate this behavior to the use of V_{ion} values less than 13.6 eV

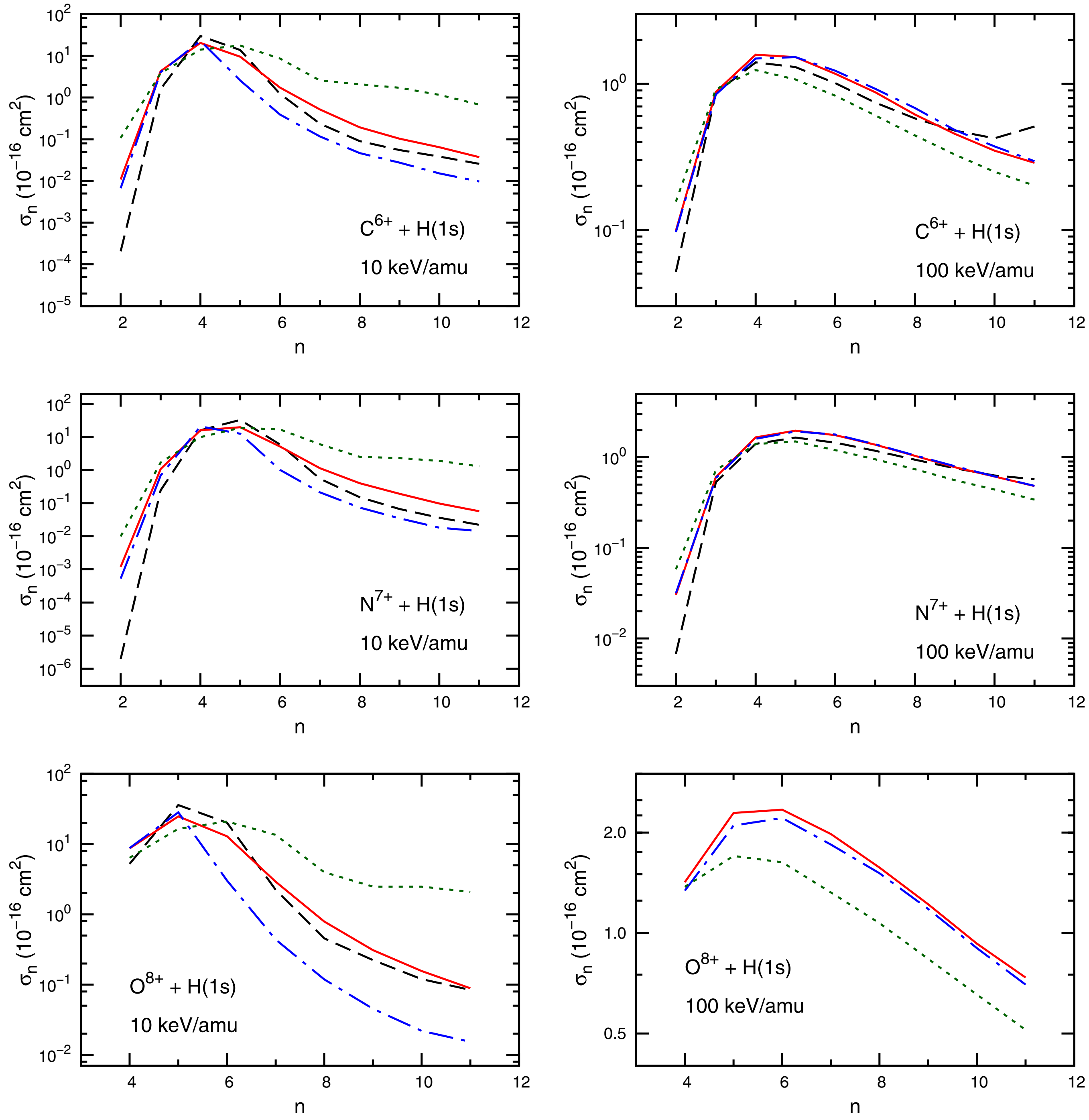

FIG. 3. (Color online) State-selective electron-capture cross sections for C^{6+}, N^{7+}, and O^{8+} collisions on ground state H(1*s*) at collision energies of 10 keV/amu (left) and 100 keV/amu (right). Lines are as in Fig. 2.

as a means to extend the radial distribution. As clearly expected from the $\sqrt{13.6/V_{\mathrm{ion}}}q^{3/4}$ scaling law, this procedure turns n distributions wider compared to the microcanonical description.

Results obtained with the hydrogenic-Z-CTMC model, on the other hand, are found to be in much better agreement with those of the AOCC method for the three collision systems in the entire energy range explored.

To further inspect these preliminary assessments, in Fig. 3 we show the n distributions at impact energies of 10 and 100 keV/amu. At low impact energies (10 keV/amu), it can be seen that the hydrogenic-E-CTMC distributions are much wider than the AOCC distributions for the three projectiles explored, while the standard microcanonical description clearly underestimates the population of high-lying n values. In contrast, the hydrogenic-Z-CTMC method provides an overall description that is in much better agreement with the AOCC results.

As we move to larger impact energies (100 keV/amu), the electron-capture channel is now fed from a much shorter

TABLE II. Hydrogenic-Z-CTMC model n-state-selective electron-capture cross sections (in units of 10^{-16} cm^{-2}) for C^{6+}, N^{7+}, and O^{8+} collisions on H(1s) at impact energies of 10, 50, and 100 keV/amu.

	C^{6+}			N^{7+}			O^{8+}		
n	10.0	50.0	100.0	10.0	50.0	100.0	10.0	50.0	100.0
2	1.09×10^{-2}	7.90×10^{-2}	9.88×10^{-2}	1.19×10^{-3}	1.96×10^{-2}	3.03×10^{-2}	3.96×10^{-4}	3.17×10^{-3}	9.11×10^{-3}
3	4.31	2.50	8.81×10^{-1}	1.07	1.26	6.07×10^{-1}	1.97×10^{-1}	4.95×10^{-1}	3.52×10^{-1}
4	2.03×10^{1}	7.32	1.58	1.59×10^{1}	6.56	1.66	8.64	4.66	1.42
5	8.37	6.33	1.52	1.97×10^{1}	8.58	1.97	2.47×10^{1}	9.50	2.29
6	1.58	3.90	1.17	5.19	6.19	1.76	1.29×10^{1}	8.70	2.34
7	5.19×10^{-1}	2.22	8.75×10^{-1}	1.14	3.77	1.38	2.91	5.86	1.98
8	1.94×10^{-1}	1.32	6.16×10^{-1}	3.99×10^{-1}	2.23	1.04	7.90×10^{-1}	3.53	1.57
9	1.03×10^{-1}	8.49×10^{-1}	4.54×10^{-1}	1.92×10^{-1}	1.39	7.78×10^{-1}	3.10×10^{-1}	2.17	1.22
10	6.43×10^{-2}	5.74×10^{-1}	3.48×10^{-1}	9.80×10^{-2}	9.34×10^{-1}	6.12×10^{-1}	1.56×10^{-1}	1.40	9.29×10^{-1}
11	3.74×10^{-2}	4.07×10^{-1}	2.87×10^{-1}	5.72×10^{-2}	6.17×10^{-1}	4.81×10^{-1}	8.87×10^{-2}	9.18×10^{-1}	7.35×10^{-1}
12	2.75×10^{-2}	3.07×10^{-1}	2.15×10^{-1}	4.26×10^{-2}	4.54×10^{-1}	3.66×10^{-1}	4.95×10^{-2}	6.58×10^{-1}	5.78×10^{-1}
13	1.70×10^{-2}	2.28×10^{-1}	1.70×10^{-1}	2.89×10^{-2}	3.33×10^{-1}	3.04×10^{-1}	3.62×10^{-2}	4.79×10^{-1}	4.91×10^{-1}
14	1.37×10^{-2}	1.74×10^{-1}	1.30×10^{-1}	1.70×10^{-2}	2.62×10^{-1}	2.44×10^{-1}	2.41×10^{-2}	3.70×10^{-1}	3.79×10^{-1}
15	8.91×10^{-3}	1.43×10^{-1}	1.20×10^{-1}	1.48×10^{-2}	2.01×10^{-1}	1.99×10^{-1}	1.66×10^{-2}	2.75×10^{-1}	3.01×10^{-1}

range of impact parameters. We note that the microcanonical description overestimates the AOCC results (only available for C^{6+} and N^{7+}). This we relate again to the compressed radial distribution which provides a physical picture of a more dense electron cloud at low impact parameters. The hydrogenic-E-CTMC, on the other hand, clearly underestimates a good fraction of the n distribution. Electron capture at these larger impact energies is strongly conditioned by the matching between the orbital velocity of the electron and that of the impinging projectile. The use of different V_{ion} values to gain radial extension mismatches the electron and projectile velocities, affecting the electron capture to high-lying levels.

Again, we note that the present hydrogenic-Z-CTMC model is in much better agreement with the AOCC results over the whole energy range. Moreover, AOCC results for $n > 10$ should be taken with caution, provided that the finite basis size employed, although extremely large, masks a fraction of the ionization probability as electron capture to high-lying levels. This is clearly seen in the tails of the AOCC distributions for C^{6+} and N^{7+} in Fig. 3.

In Table II, we present the hydrogenic-Z-CTMC n-state-selective electron-capture cross sections to levels $n = 2$ to 15 for the three projectiles considered at impact energies of 10, 50, and 100 keV/amu.

B. State-selective electron capture in C^{6+}, N^{7+}, and O^{8+} collisions on $H^*(n = 2)$

As already stated in the Introduction, electron-capture data for $H^*(n = 2)$ targets are of particular relevance to charge-exchange diagnostics. In this section, we compare the results predicted at the state-selective level by the microcanonical CTMC, hydrogenic-Z-CTMC, and AOCC methods. Based on the results shown in the previous section, we do not include any hydrogenic-E-CTMC results at this point.

TABLE III. Hydrogenic-Z-CTMC model n-state selective electron-capture cross sections (in units of 10^{-16} cm^{-2}) for C^{6+}, N^{7+}, and O^{8+} collisions on $H^*(n = 2)$ at impact energies of 10, 50, and 100 keV/amu.

	C^{6+}			N^{7+}			O^{8+}		
n	10.0	50.0	100.0	10.0	50.0	100.0	10.0	50.0	100.0
2	1.83×10^{-4}	1.10×10^{-3}	2.02×10^{-3}	1.90×10^{-4}	6.00×10^{-5}	1.82×10^{-3}	1.15×10^{-4}	4.17×10^{-5}	2.30×10^{-4}
3	5.85×10^{-3}	5.92×10^{-2}	2.97×10^{-2}	2.35×10^{-3}	1.90×10^{-2}	2.80×10^{-2}	2.05×10^{-4}	4.85×10^{-3}	9.45×10^{-3}
4	3.075×10^{-1}	3.55×10^{-1}	7.75×10^{-2}	4.40×10^{-2}	2.00×10^{-1}	7.65×10^{-2}	8.13×10^{-3}	9.50×10^{-2}	4.88×10^{-2}
5	4.90	8.50×10^{-1}	1.02×10^{-1}	1.15	6.35×10^{-1}	1.07×10^{-1}	2.63×10^{-1}	4.30×10^{-1}	1.08×10^{-1}
6	2.82×10^{1}	1.22	1.05×10^{-1}	1.01×10^{1}	1.17	1.17×10^{-1}	3.08	9.72×10^{-1}	1.50×10^{-1}
7	6.77×10^{1}	1.42	9.57×10^{-2}	3.92×10^{1}	1.52	1.11×10^{-1}	1.75×10^{1}	1.57	1.72×10^{-1}
8	8.82×10^{1}	1.35	7.92×10^{-2}	7.95×10^{1}	1.72	9.62×10^{-2}	5.25×10^{1}	2.02	1.72×10^{-1}
9	7.85×10^{1}	1.30	6.65×10^{-2}	9.90×10^{1}	1.72	8.22×10^{-2}	9.35×10^{1}	2.17	1.55×10^{-1}
10	5.57×10^{1}	1.10	5.37×10^{-2}	9.00×10^{1}	1.60	6.82×10^{-2}	1.10×10^{2}	2.25	1.45×10^{-1}
11	3.65×10^{1}	9.45×10^{-1}	4.32×10^{-2}	6.67×10^{1}	1.47	5.57×10^{-2}	9.65×10^{1}	2.15	1.25×10^{-1}
12	2.32×10^{1}	8.02×10^{-1}	3.55×10^{-2}	4.47×10^{1}	1.27	4.62×10^{-2}	7.38×10^{1}	2.02	1.03×10^{-1}
13	1.55×10^{1}	6.82×10^{-1}	2.97×10^{-2}	2.92×10^{1}	1.15	3.90×10^{-2}	5.00×10^{1}	1.80	8.95×10^{-2}
14	1.07×10^{1}	5.85×10^{-1}	2.45×10^{-2}	1.92×10^{1}	1.00	3.30×10^{-2}	3.25×10^{1}	1.60	7.85×10^{-2}
15	7.75	5.12×10^{-1}	2.22×10^{-2}	1.35×10^{1}	8.72×10^{-1}	2.82×10^{-2}	2.20×10^{1}	1.40	6.77×10^{-2}

Provided that an electron bound in the H*($n = 2$) orbital ($V_{\text{ion}} = 3.4$ eV) could be either found in the $2s$ state or the $2p$ state, the cross section for τ process is defined as

$$\sigma^{\tau}(n = 2) = \tfrac{1}{4}\sigma^{\tau}(2s) + \tfrac{3}{4}\sigma^{\tau}(2p). \qquad (7)$$

In Fig. 4 we show the electron-capture cross sections to levels $n = 3$ to 9, $n = 4$ to 10, and $n = 5$ to 12 for C^{6+}, N^{7+}, and O^{8+}, respectively. These are represented as a function of impact energy in the 10–150 keV/amu range. According to the $\sqrt{13.6/V_{\text{ion}}}q^{3/4}$ scaling law, maxima in the n distributions are expected at $n = 8$, 9, and 10, respectively.

In the first place, we note that, in contrast with what was shown in the previous section for H(1s), the microcanonical CTMC and the hydrogenic-Z-CTMC models provide results which are in very good agreement with each other along the whole energy range explored, as well as with the AOCC data. We have checked that the agreement between both classical results stands for the separate contributions of the $2s$ and $2p$ states.

It should be noticed that the AOCC data overestimate the classical models as the impact energy increases. This situation is more evident for the higher n levels considered. We again ascribe this feature to the finite-basis-size effect which masks a fraction of the ionization probability into electron capture to the highest n levels considered [26], as already stated in the previous section.

In Table III, we present the hydrogenic-Z-CTMC n-state-selective electron-capture cross sections to levels $n = 2$ to 15 for the three projectiles considered at impact energies of 10, 50, and 100 keV/amu.

Finally, in Fig. 5, we examine the population of the l substates for electron capture to $n = 3$ to 9, $n = 4$ to 10, and $n = 5$ to 12 in C^{6+}, N^{7+}, and O^{8+}, respectively, at an impact energy of 10 keV/amu. We find nearly no difference between the two classical models and good agreement with the quantal model. As expected, large l values are mainly populated at this impact energy and, as a general trend, the classical models seem to underestimate the population of the $l = 0$ substates given by the AOCC as the n values increase.

C. Line emission cross sections in C^{6+}, N^{7+}, and O^{8+} collisions on H(1s) and H*($n = 2$)

In this section, we sanalyze the line emission cross sections that provide information on the photon emission that follows the electron capture processes studied in the previous sections. Results obtained with the hydrogenic-Z-CTMC model are displayed since they have been proven to be reliable and cover all systems and energies. Photon cascades from levels up to $n = 30$ are included in all line emission cross-section calculations.

In Fig. 6 we show the Ly-α, Ly-β and Ly-γ lines as a function of impact energy. For the projectiles under study, the energy of these lines corresponds to the x-ray region. In order to highlight the relative role of the H(1s) and H*($n = 2$) targets in the fusion reactor environment, cross sections corresponding to the H*($n = 2$) target are multiplied by a factor of 0.01. By so doing, the estimated relative abundance of H*($n = 2$) is taken into account since it is found to be on the order of 1% during neutral beam heating and fueling of fusion reactors [20–23]. It can be seen that the Ly-α for H(1s) provides the dominant contribution throughout the impact-energy range considered despite the fact that the photonic emission arising from H*($n = 2$) gains intensity as the impact energy decreases. This is simply because the Lyman-α cross section is approximately 90% of the overall total electron-capture cross section for each

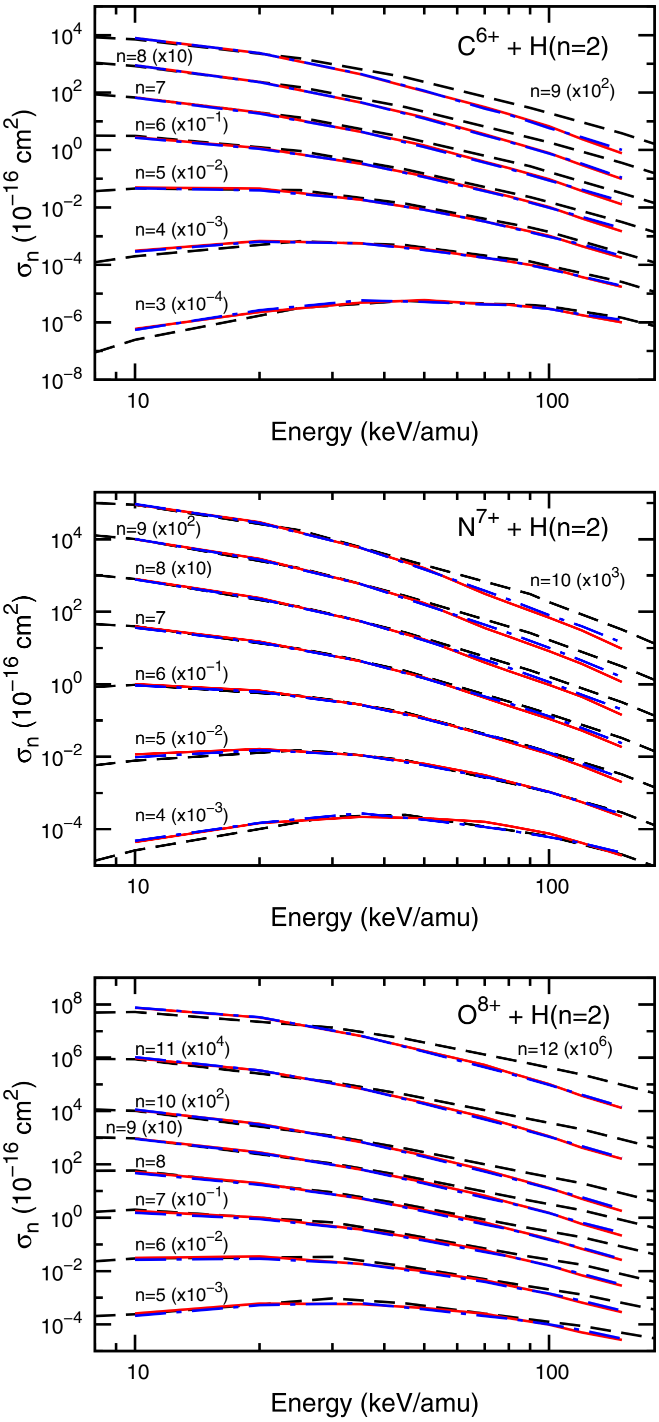

FIG. 4. (Color online) n-state-selective capture cross section as a function of the projectile energy following C^{6+}, N^{7+}, and O^{8+} collisions on H*($n = 2$). Theories are shown by red-solid line for hydrogenic-Z-CTMC, blue dashed-dotted line for microcanonical-CTMC, and black dashed line for AOCC model [26,27].

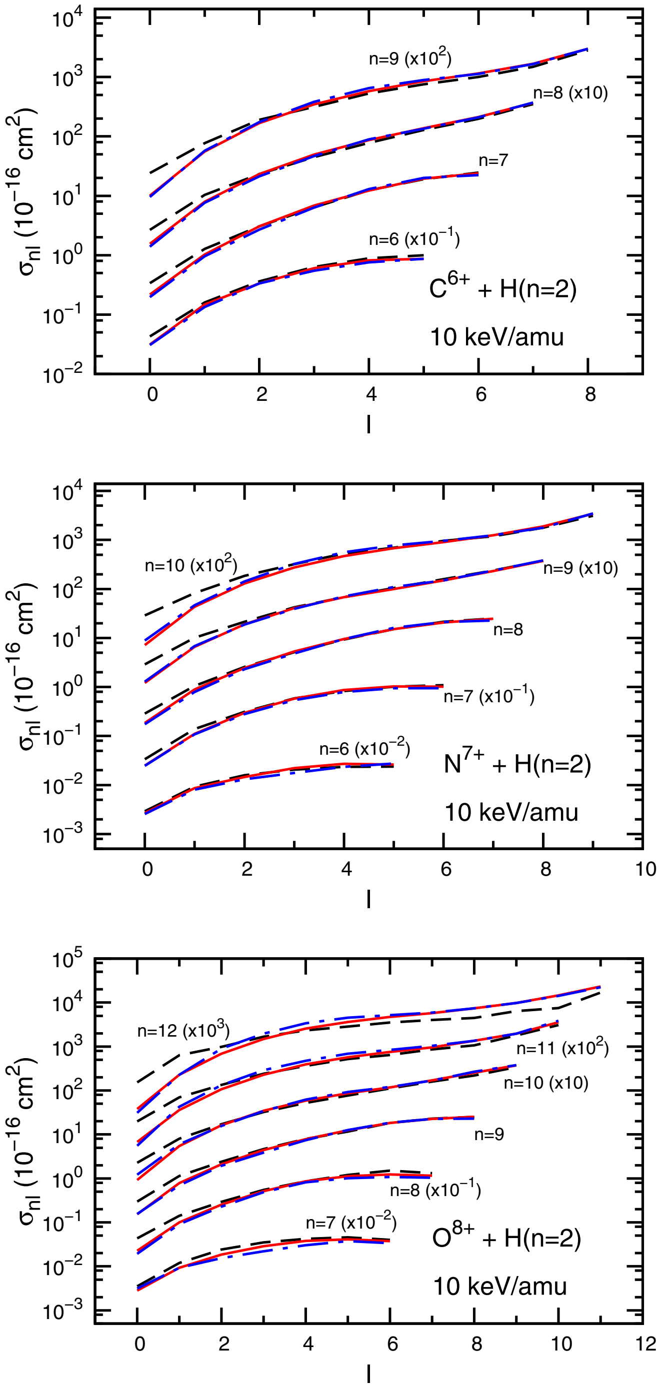

FIG. 5. (Color online) l-state-selective capture cross sections for electron capture to $n = 3$ to 9, $n = 4$ to 10, and $n = 5$ to 12 in C^{6+}, N^{7+}, and O^{8+}, respectively, at an impact energy of 10 keV/amu. Lines are as in Fig. 4.

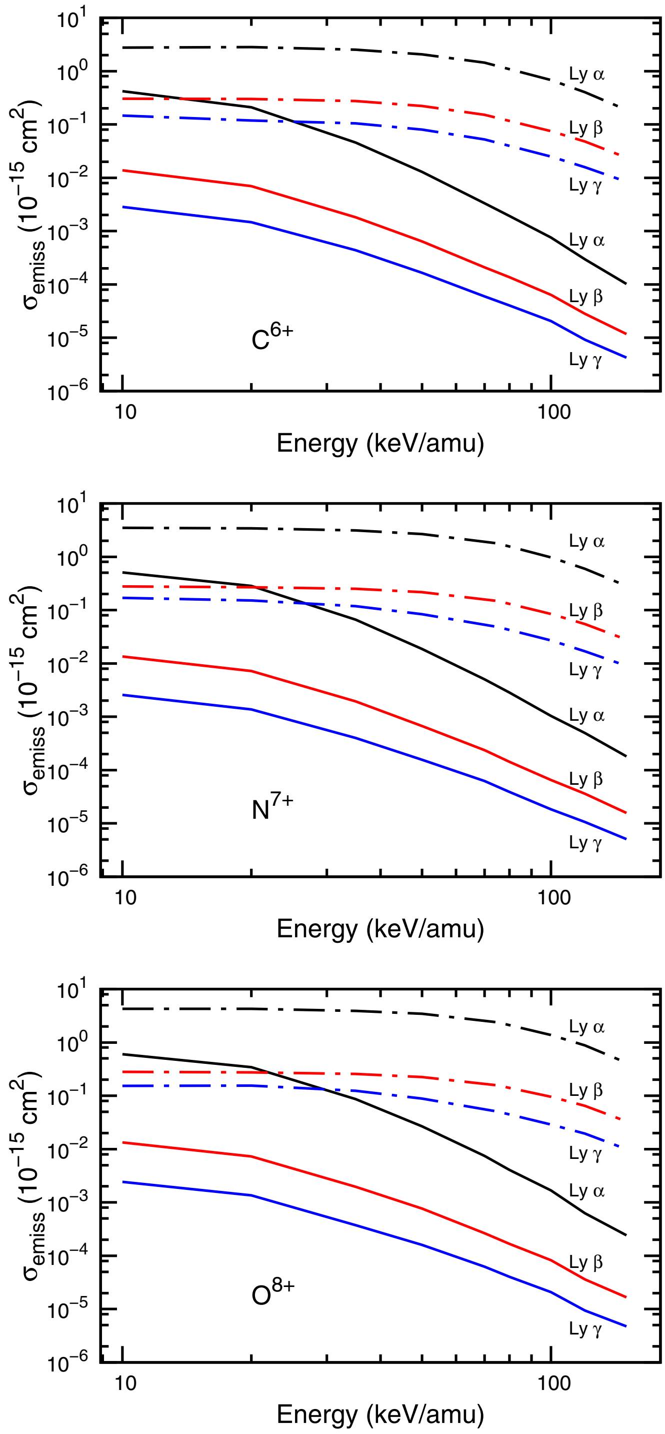

FIG. 6. (Color online) Line emission cross sections in the x-ray spectral range as a function of impact energy for C^{6+}, N^{7+}, and O^{8+} collisions on H(1s) (dashed lines) and H*($n = 2$) (solid lines). The H*($n = 2$) cross sections are reduced to 1% of their value to mimic the power reactor environment.

reaction due to a very low hardness ratio at these collision energies.

A completely different behavior is observed when analyzing transitions involving photon transitions in the visible range relevant to plasma diagnostics. In Fig. 7 we show the most intense lines for each projectile (8 → 7, 10 → 8, and 11 → 9 for C^{6+}; 9 → 8, 10 → 9, and 11 → 10 for N^{7+}; and 9 → 8, 10 → 9, and 11 → 10 for O^{8+}). Again, line emission cross sections corresponding to the H*($n = 2$) target have been multiplied by a factor of 0.01 to mimic the fusion reactor environment. In these cases, we note that even the small 1% fraction of H*($n = 2$) provides the dominant photonic contribution at impact energies below about 35 keV/amu. This energy range encompasses the central plasma core temperature

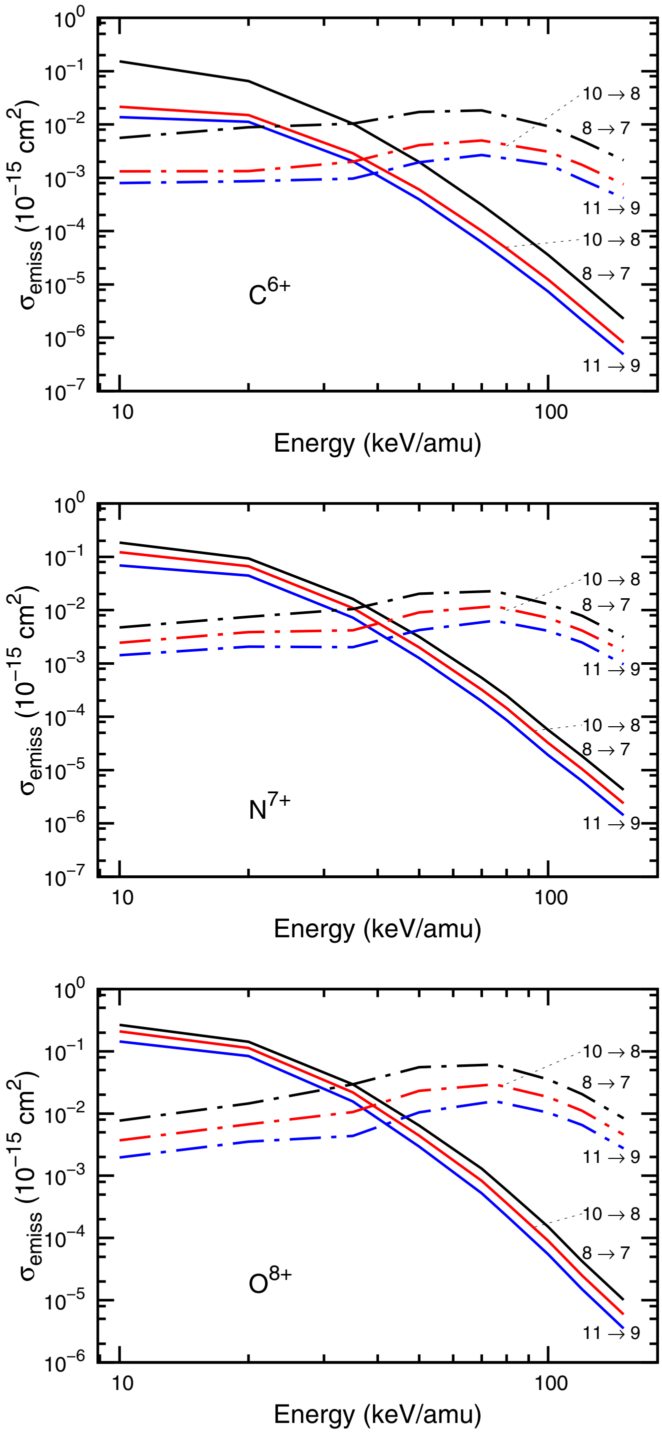

FIG. 7. (Color online) Main line emission cross sections in the visible spectral range as a function of impact energy for C^{6+}, N^{7+}, and O^{8+} collisions on H(1s) (dashed lines) and H*($n = 2$) (solid lines). The H*($n = 2$) cross sections are reduced to 1% of their value to mimic the power reactor environment.

of about 10 keV/amu and the half and one-third energy components of the ca. 50 keV/amu heating and fueling neutral deuterium beam.

At energies above 35 keV/amu, visible line emission after electron capture from H(1s) dominates. This is because ionization, not electron capture, determines the electron removal process for collision speeds that exceed the nominal speed of the target electron. Such energies are 6.25 keV/amu for H*($n = 2$) and 25 keV/amu for H(1s). As a result, the line emission cross section for H*($n = 2$) decreases rapidly at the higher energies due to the rapidly declining electron capture. Unlike in the Lyman cases presented above, the visible line emission for H(1s), resulting from transitions between high-lying n levels have a slight maximum around 70 keV/amu, which is the energy at which the state-specific capture cross sections from H(1s) to the originating level of the photon emission display maxima (see Fig. 2). We point out that, as the ionization channel gains significance, the n-level capture cross sections broaden considerably, as seen in Figs. 3 and 4. This broadening of n-level cross sections also increases the contribution from cascades, accentuating the line emission.

IV. CONCLUSIONS

In this paper we have presented a hydrogenic CTMC method, conceived to provide accurate momentum and radial distributions for H(1s) and H*($n = 2$). This method was developed so that conventional binning procedures to determine the (n,l) cross sections after electron capture correspond to the energy defects of the specific state-to-state reactions, unlike that for the hydrogenic-E-CTMC method. Furthermore, the new method is consistent with physical observations provided by momentum spectroscopy measurements that show a sharp step in the longitudinal momentum distributions due to the electron capture to the continuum mechanism [33].

Electron-capture reactions with C^{6+}, N^{7+}, and O^{8+} projectiles at impact energies in the range 10–150 keV/amu have been studied in order to evaluate the present model and check its performance against the standard microcanonical CTMC method, the hydrogenic-E-CTMC method, and the AOCC model. For H(1s), state-selective electron-capture data provided by the present model were found to be in much better agreement with AOCC than those obtained by means of the standard microcanonical and the hydrogenic-E-CTMC methods. Advantages seem to be connected with the precise radial distribution that, in contrast to the hydrogenic-E-CTMC, is achieved by considering the correct V_{ion} in all expansion terms.

Results for excited hydrogen are less sensitive to the initialization procedure. The standard microcanonical CTMC model provides results of similar quality to those provided by the more elaborate and computation-time-demanding hydrogenic-Z-CTMC method. For this target, classical results are in very good agreement with the AOCC results, except on the population of high-lying states at large impact energies. Here, the finite basis size effect of the quantal method seems to lead to an overestimation of electron capture into those high n levels.

Finally, we presented line emission cross sections corresponding to the Ly-α, Ly-β, and Ly-γ transitions, which for the projectiles under study populate the x-ray spectral range, as well as those corresponding to transitions that contribute to the visible spectral range. Present results show that charge-exchange diagnostics that are based on the observation of visible transitions, demonstrate the dominant and crucial role that even a tiny fraction of H$^*(n = 2)$ can have at low impact energies (ca. 10 keV/amu).

Collaboration programs including different methodologies, like the one recently pushed and published by Igenbergs *et al.* [26], are encouraged. No doubt these will surely help to refine present databases of state-selective charge-exchange cross sections on H(1s) and H$^*(n = 2)$ of potential relevance for plasma physicists and astrophysicists.

ACKNOWLEDGMENT

Work at Universidad Nacional del Sur is supported by Grants No. PGI 24/F059 and No. PIP 112-201101-00749 of CONICET (Argentina).

---

[1] R. Abrines and I. C. Percival, Proc. Phys. Soc., London **88**, 873 (1966).
[2] R. E. Olson and A. Salop, Phys. Rev. A **16**, 531 (1977).
[3] R. E. Olson, Phys. Rev. A **24**, 1726 (1981).
[4] R. E. Olson, in *Handbook of Atomic, Molecular, and Optical Processes*, edited by G. Drake (Springer, New York, 2006), Chap. 58.
[5] D. Eichenauer, N. Grun, and W. Scheid, J. Phys. B: At. Mol. Phys. **14**, 3929 (1981).
[6] D. J. W. Hardie and R. E. Olson, J. Phys. B: At. Mol. Phys. **16**, 1983 (1983).
[7] J. S. Cohen, J. Phys. B: At. Mol. Phys. **18**, 1759 (1985).
[8] C. L. Kirschbaum and L. Wilets, Phys. Rev. A **21**, 834 (1980).
[9] R. E. Olson, Phys. Rev. A **36**, 1519(R) (1987).
[10] M. L. McKenzie and R. E. Olson, Phys. Rev. A **35**, 2863 (1987).
[11] A. E. Wetmore and R. E. Olson, Phys. Rev. A **38**, 5563 (1988).
[12] R. E. Olson, J. Ullrich, and H. Schmidt-Böcking, Phys. Rev. A **39**, 5572 (1989).
[13] V. J. Montemayor and G. Schiwietz, Phys. Rev. A **40**, 6223 (1989).
[14] L. Meng, C. O. Reinhold, and R. E. Olson, Phys. Rev. A **40**, 3637 (1989).
[15] C. J. Wood and R. E. Olson, Phys. Rev. A **59**, 1317 (1999).
[16] M. Alessi, N. D. Cariatore, P. Focke, and S. Otranto, Phys. Rev. A **85**, 042704 (2012).
[17] N. D. Cariatore and S. Otranto, Phys. Rev. A **88**, 012714 (2013).
[18] http://www.ccfe.ac.uk/JET.aspx
[19] www.iter.org
[20] R. C. Isler, Plasma Phys. Control. Fusion **36**, 171 (1994).
[21] R. Hoekstra, H. Anderson, F. W. Bliek, M. von Hellermann, C. F. Maggi, R. E. Olson, and H. P. Summers, Plasma Phys. Control. Fusion **40**, 1541 (1998).
[22] H. Anderson, M. G. von Hellermann, R. Hoekstra, L. D. Horton, A. C. Howman, R. W. T. Konig, R. Martin, R. E. Olson, and H. P. Summers, Plasma Phys. Control. Fusion **42**, 781 (2000).
[23] R. C. Isler and R. E. Olson, Phys. Rev. A **37**, 3399 (1988).
[24] Wolfgang Fritsch and C. D. Lin, Phys. Rev. A **29**, 3039 (1984).
[25] Nobuyuki Toshima, Phys. Rev. A **50**, 3940 (1994).
[26] K. Igenbergs, J. Schweinzer, A. Veiter, L. Perneczky, E. Frühwirth, M. Wallerberger, R. E. Olson, and F. Aumayr, J. Phys. B: At., Mol. Opt. Phys. **45**, 065203 (2012).
[27] K. Igenbergs, Ph.D. thesis, Vienna University of Technology, 2011.
[28] C. O. Reinhold and C. A. Falcon, Phys. Rev. A **33**, 3859 (1986).
[29] S. Otranto and R. E. Olson, Phys. Rev. A **83**, 032710 (2011).
[30] S. Otranto, N. D. Cariatore, and R. E. Olson, Phys. Rev. A **90**, 062708 (2014).
[31] R. L. Becker and A. D. MacKellar, J. Phys. B: At. Mol. Phys. **17**, 3923 (1984).
[32] S. Schippers, P. Boduch, J. van Buchem, F. W. Bliek, R. Hoekstra, R. Morgenstern, and R. E. Olson, J. Phys. B: At., Mol. Opt. Phys. **28**, 3271 (1995).
[33] Th. Weber, Kh. Khayyat, R. Dörner, V. D. Rodríguez, V. Mergel, O. Jagutzki, L. Schmidt, K. A. Müller, F. Afaneh, A. González, and H. Schmidt-Böcking, Phys. Rev. Lett. **86**, 224 (2001).